Available online at www.sciencedirect.com

ScienceDirect

Journal of Magnesium and Alloys 10 (2022) 1235–1241

www.elsevier.com/locate/jma

Full Length Article

The evolution of coarse grains and its effects on weakened basal texture during annealing of a cold-rolled magnesium AZ31B alloy

Xin Wang, Dikai Guan*

Department of Materials Science and Engineering, University of Sheffield, Sheffield S13JD, UK

Received 21 May 2021; received in revised form 27 July 2021; accepted 29 August 2021
Available online 10 October 2021

Abstract

The nucleation, grain growth of 34 coarse grains during annealing were tracked using a quasi-*in-situ* EBSD method. These 34 coarse grains had different orientations and most grains were non-basal orientated. No preferable grain growth or special types of grain boundaries were identified. Only 9 coarse grains nucleated from deformed grain boundaries due to initial large grain size and limited grain boundary volume fraction. The main nucleation site of 34 coarse grains was dislocation cells or subgrains in deformed grain interiors. Their recrystallisation behaviour can be illustrated by abnormal subgrain growth (AsGG) rarely reported in Mg alloys. The coarse basal grains showed no growth advantage in terms of grain size or number over other non-basal grains, leading to a weak basal texture in AZ31B alloy.

Keywords: Magnesium alloy; EBSD; Annealing; Recrystallisation; Grain growth.

1. Introduction

Different approaches have been used to weaken the basal texture in Mg alloys to improve their formability [1–4]. The addition of rare earth elements and/or Ca introduce a special "RE texture", leading to weakening basal texture [5–8]. Static recrystallisation (SRX) of non-rare earth (non-RE) containing Mg alloys normally leads to strong basal texture [2,9,10]. Dynamic recrystallisation (DRX) can introduce some non-basal grains at the early stage [11], but these non-basal orientations were consumed after full SRX or DRX [10–13].

Nevertheless, basal texture weakening did occur in non-RE Mg alloys after SRX or hot rolling at high temperatures [14–17]. Huang et al. [16,17] reported that the basal texture intensity after annealing was significantly decreased when the finishing hot rolling temperature was 525 °C in AZ31 alloy. The enhanced non-basal slip activities at the rolling temperature of 525 °C may result in non-basal nuclei [17]. However, the weakening mechanism in these studies was not fully investigated.

Orientated/preferential growth of recrystallised grains can control the final recrystallised texture. In pure Mg and non-RE alloys like AZ31, basal grains normally dominated the grain growth stage, resulting in strong basal texture [8,12,13]. The coarse and/or abnormal grains were the main source of high basal texture intensity in non-RE Mg alloys [12,13,18]. It is accepted that these coarse basal grains are nucleated from deformed grain boundaries (GBs) via strain-induced grain boundary migration (SIBM) by examining a single point during partial recrystallisation [19]. However, tracking the growth of coarse/abnormal grains and determining their nucleation sites have not been systematically reported but are urgently needed to illustrate recrystallisation mechanisms. If deformed GBs are the main source of these coarse basal grains, what would happen if the starting material has a low volume fraction of GBs (e.g., a big initial grain size before deformation)?

To address these issues, a quasi-*in-situ* EBSD method was used to record the full recrystallisation process of the same sampling area in AZ31B alloy with a large initial average grain size. The nucleate sites, growth behaviour of coarse

* Corresponding author.
E-mail address: dikai.guan@sheffield.ac.uk (D. Guan).

https://doi.org/10.1016/j.jma.2021.08.026

grains and their contribution to the final texture were accurately identified.

2. Experimental procedure

A commercial hot-rolled AZ31B alloy cuboid supplied by Magnesium Elektron was used in this work. A rectangular plate 60 (RD) × 30 (TD) × 6 (ND) mm^3 was cut for cold rolling and heat treatment (RD: rolling direction, TD: transverse direction, ND: normal direction). Solid solution treatment was carried out in a tube furnace with continuous argon flow at 510 °C for 24 h, followed by cold water quenching. The heat-treated sample was then cold rolled with a reduction of 13% in one pass. The cold-rolled sample was well ground and polished. EBSD was performed using a JSM-7900F Schottky FESEM fitted with Oxford Instruments Symmetry EBSD detector. For the as-received sample, the step size was 0.5 μm. The step size of a sample after solid solution treatment, cold rolling and annealed at 350 °C (designated as SCA350) for 2 h was 2 μm. The quasi-*in-situ* EBSD collected data from a large area of ~2.1 mm^2 from the middle part of ND-RD plane. The step size for cold-rolled sample was 0.4 μm, while for annealed samples was 0.9–1.35 μm. The EBSD data were analysed using AZTecCrystal software. The EBSD scans were taken from the same sampling area after 270 s, 630 s, 1290 s, 2000 s, 3200 s, 6800 s and 14,000 s annealing at 350 °C. Fiducial marks were made on the surface of the cold-rolled sample after OPS polishing. Thus the area scanned for EBSD was precisely relocated after further annealing to allow re-scanning of exactly the same area. After every EBSD run, the sample was transferred into an argon glove box and sealed in a small aluminium vial. Subsequent annealing was undertaken in a tube furnace with flowing argon with the sample contained in the vial for protection. After annealing, water quenching was undertaken, with the vial providing protection from the water, such that the region of interest on the surface of the sample was protected. To remove any oxide from the surface of interest for the next EBSD scan, the annealed sample was given a mild polish using 40 nm OPS suspension. The thickness reduction after this mild polishing was less than 1 μm, measured by a micrometre [20].

In general, individual grains with a grain orientation spread (GOS) less than 1.2° were determined as recrystallised grains in this work. In addition, because quasi-*in-situ* EBSD tracking method was used in this work, all the new recrystallised grains can be easily separated from residual deformed grain areas after comparing EBSD maps at different annealing stages if GOS did not work perfectly for identifying a very small amount of recrystallised grains.

3. Results and discussion

3.1. Microstructure of as-received and SCA350 samples

Fig. 1(a) presents an Inverse Pole Figure (IPF) EBSD image of the as-received AZ31 sample. It consists of 4312 grains and its average grain size was 7.6 μm. As shown in Fig. 1(c), the as-received sample presented a typical basal texture with an intensity of ~10.9 mud. Fig. 1(b) gives an IPF image of sample SCA350. It contains 3254 grains and its average grain size is 17.8 μm. The average grain size of SCA350 sample is nearly three times of as-received sample. The reason for this was the initial average grain size of SCA350 before cold rolling is larger than 200 μm (Fig. S1 in supplementary material). Thus, the final recrystallised grain size of SCA350 was coarser than as-received sample [19]. A typical but weak basal texture can be still found in SCA350 and its intensity is only 4.6 mud. Scattered texture components were distributed randomly across RD and TD directions, which reduced the basal texture intensity. In both IPF maps, coarse grains much bigger than average grain size can be easily observed. In the following sections, the evolution of these coarse grains from the beginning of appearance to the following grain growth will be fully analysed. The reasons for texture weakening of the whole sample after annealing will be reported separately in the future work.

3.2. Microstructure after cold rolling for quasi-in-situ EBSD examination

Fig. S2 gives a large area IPF EBSD map of the sample after solid solution treatment and cold rolling. Shear bands, tension twins and double twins were the main deformation microstructures in this cold-rolled sample. The effect of individual deformation microstructure on the nucleation and grain growth of recrystallised grains will be reported in another paper and will not be discussed here.

3.3. The effect of coarse grains on texture formation

Fig. S3(a–g) provides the entire annealing process of the same sampling area in Fig. S2. The only residual deformed areas are marked as A and B in Fig. 2(a) showing the IPF EBSD map of sample SCA350 after annealing for a total time of 14,000 s annealing at 350 °C. This EBSD map in Fig. 2(a) consists of 4197 recrystallised grains and its average grain size is around 21.1 μm. Again, the (0002) pole figure containing only recrystallised grains shows a weak basal texture with the intensity of 4.6 mud (Fig. 2(d)). The reason for this is non-basal grains survived during grain growth and can be easily found even after 14,000 s annealing. It is evident to observe that a considerable number of coarse grains were distributed amongst the fine grains.

The basal texture intensity of sample SCA350 after 14,000 s annealing was sharply reduced compared to as-received sample (Fig. 1(c)). To investigate the coarse grains evolution and their contribution to final texture formation, 34 coarse grains with grain size larger than 70 μm were selected and presented in Fig. 2(b) and they occupied around 9% of the whole EBSD map. As seen in the scattered pole figure Fig. 2(e), the orientations of most grains were quite different and non-basal. Although the texture intensity of these 34 grains was up to 15.5 mud, this heavily depended on the number of grains included and the area of individual grains.

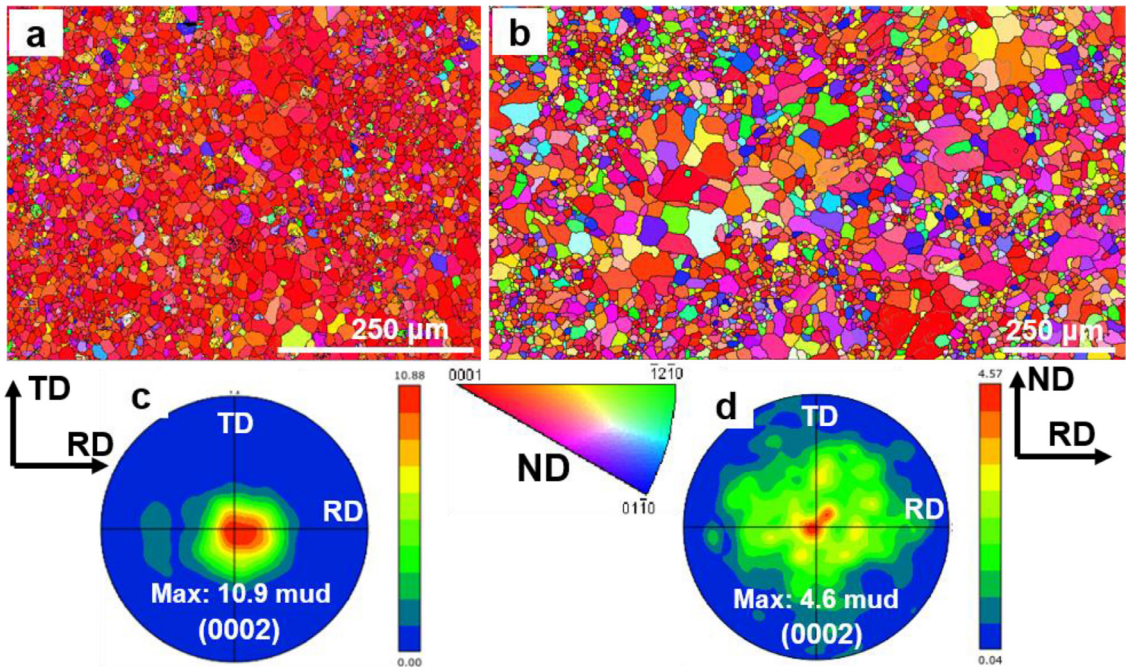

Fig. 1. (a) EBSD IPF image of a large area from as-received AZ31B, (b) EBSD IPF image of a large area from sample SCA350 after 2 h annealing, (c) (0002) pole figure of (a), and (d) (0002) pole figure of (b).

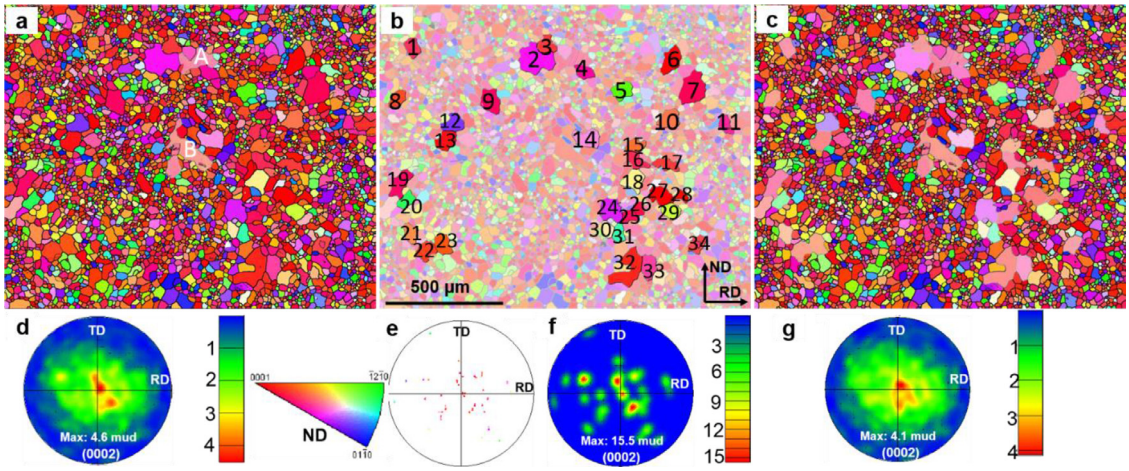

Fig. 2. EBSD IPF image of a large area from sample SCA350 after 14,000 s annealing (a) all recrystallised grains, (b) only 34 coarse grains with grain size bigger than 70 μm, (c) recrystallised grains with grains size smaller than 70 μm. (d) (0002) pole figure of (a), (e) and (f) scattered and contoured (0002) pole figures of (b), and (0002) pole figure of (c).

Thus, the intensity in Fig. 2(f) cannot indicate there were texture components. Fig. 2(c) shows the EBSD map without the 34 coarse grains and 2 residual deformed areas of A and B. The corresponding (0002) pole figure is shown in Fig. 2(g). The texture morphologies of the whole sampling area with and without these 34 coarse grains were quite similar, but the intensity of basal texture of the whole sampling area was slightly lower without the coarse grains. This indicated the existence of coarse grains can enhance the basal texture of the sample to some extent. It means further extending the annealing time of sample SCA350 may enhance the basal texture of the sample. Thus, optimising the heat treatment parameters is an efficient way to prevent strong basal texture caused by coarse grains with basal orientations.

3.4. The nucleation and growth of coarse grains

Recrystallised grains can be nucleated at several deformation sites where the stored energy is high: i.e., shear bands, deformation twins, second phase particles, deformed GBs [4,7,13,21]. The literature shows the former three deformation sites nucleate grains with random orientations, while the latter one normally produces orientations similar to deformed basal grains. For non-RE containing Mg alloys like AZ31, the final recrystallised texture was usually dominated by strong

basal texture although abundant of shear bands, deformations twins were observed before recrystallisation [22]. On the contrary, only weak basal texture was produced in this AZ31B alloy, and the coarse grains had various grain orientations. Therefore, it is key to identify the nucleation sites and growth behaviour of coarse grains in Fig. 2(b). After careful examination, 5 types of nucleation sites of these 34 coarse grains can be identified. Table S1 lists the nucleation sites of coarse grains, their misorientation with deformed grains, and their first appearance time.

9 coarse grains originated from deformed GBs, 3 grains from shear bands, 1 grain from double twin network junctions, 1 grain from a second phase particle, and 20 grains from dislocation cells or subgrains distributed within the deformed parent grains. The recrystallisation mechanism at the dislocation cells or subgrains can be illustrated by the abnormal subgrain growth (AsGG) which has been proposed as the nucleation mechanism for recrystallisation in Al and Cu alloys [23–27]. However to our best knowledge, recrystallisation due to AsGG was rarely reported in Mg alloys. Nevertheless, AsGG was found to be the main recrystallisation mechanism for recrystallised coarse grains in this work. Fig. 3 shows the evolution of typical coarse grains originated from the former 4 nucleation sites, and Fig. 4 presents 2 coarse grains nucleated from subgrains. The evolution of all other coarse grains was provided in Figs. S4–8. It should be noted the low angle grain boundaries (LAGBs) were marked by thin white lines while high angle grain boundaries (HAGBs) were marked by thick black lines in most EBSD images when necessary.

As shown in Fig. 3(a1–a7), grain 25 was first observed after annealing 630 s (marked by a white arrow in Fig. 3(a2)), and it nucleated from the deformed grain boundary. This was confirmed in Fig. 3(a1) where no visible recrystallised grain can be detected around this deformed GB when the sample was annealed for 270 s. Grain 25 grew rapidly and consumed the deformed grains after annealing 1290 s. Its growth was restricted when grain 25 met other adjacent recrystallised grains. Fig. 3(b1) shows an area of intensive shear bands due to heavy local deformation. After annealing for 270 s, grain 29 was detected (see the white arrow in Fig. 3(b2)). It started to consume deformed parent grain, tension twins and small recrystallised grains during the annealing process (Fig. 3(b3–b8)). The corresponding band contrast EBSD images of Fig. 3(b1–b4) were shown in Fig. S9 where the original distribution and subsequent disappearance of shear bands could be tracked easily. Fig. 3(c1) presents a deformed grain mainly consisting of double twin networks. Small recrystallised grain 3 emerged at double twin junctions after 270 s annealing (see the white arrow in Fig. 3(c2)). This grain managed to grow out of the twin boundaries (Fig. 3(c4)) and consumed the deformed grain quickly (Fig. 3(c5–c8)). This double twin recrystallisation behaviour was also systematically reported in our previous Mg WE43 alloy work [20]. Fig. 3(d2) firstly shows the appearance of grain 23 after annealing 1290 s. Fig. 3(d1) shows the unindexed dark area marked by the white arrow in Fig. 3(d1) can be attributed to a second phase particle. Thus, grain 23 was nucleated from the second phase particle. It grew slowly at the early stage of the recrystallisation process but it quickly expanded into deformed parent grain when the annealing time was further extended to 6800 s. As listed in Table S1, coarse recrystallised grains originated from shear bands and double twin networks nucleated earlier than deformed GBs.

Regarding 20 coarse grains recrystallised by AsGG, their nucleation time varied. 2 coarse grains firstly detected after annealing for 1290 s and 3200 s were selected to illustrate the recrystallisation process. Fig. 4(a2) shows the large grain 5 after 1290 s annealing. This grain cannot be found in the same sampling area even after 630 s annealing at 350 °C (Fig. 4(a1)). It was evident to find substructures/dislocation cells in the deformed grain interior. Therefore, grain 5 was nucleated by the abnormal growth of subgrains as described above. Fig. 4(b1–b4) presents the nucleation and growth process of grain 14 nucleated by AsGG. Grain 14 did not appear even after 2000 s annealing. However, due to the large deformed area around the recrystallised grains nucleated by AsGG, these grains grew quickly by consuming the deformed parent grains and small recrystallised grains originated from other deformation sites (Fig. 4(a2–a6), Fig. 4(b2–b4)). More examples can be found in Fig. S6(c1–c3), grain 18 nucleated by AsGG was first observed even after 6800 s annealing, but it swiftly expanded into its deformed parent grain and grew from 17.7 to 91.5 μm. It should be noted that AsGG is different from the classical abnormal grain growth (AGG) behaviour. It is widely recognised that AGG occurs after primary recrystallisation when the microstructure becomes unstable and a few grains may grow excessively, consuming the smaller recrystallised grains, so sometimes AGG is known as secondary recrystallisation [19]. However, AsGG reported in this work has been proposed as the nucleation mechanism during primary recrystallisation. In other words, AsGG occurs before the completion of primary recrystallisation, and mainly consumed the adjacent deformed parent grain areas rather than small recrystallised grains when the recrystallised nucleated by AsGG grew up.

Several mechanisms have been proposed to explain the formation of coarse grains: (1) different mobility and energy of high and low angle boundaries [12], (2) grain size advantage of some orientated grains emerged during the early recrystallisation process and dominated the later grain growth stage [13], (3) boundary pinning induced by solute and/or Zener drag, (4) preferential growth of recrystallised grains [8], (5) fast growth rate of basal grains due to residual dislocation density gradient [18,28]. According to the pole figure of all the coarse recrystallised grains (Fig. 3(e)) and misorientation angle/axis between recrystallised grains and corresponding deformed grains listed in Table S1, no orientated/preferred grain growth or special types of GBs was observed amongst the 34 coarse recrystallised grains. Moreover, Fig. 5(a) shows only 6 out of 34 coarse grains had the basal orientation (defined by the angle differences of 0–20° between their *c*-axis and ⟨0001⟩ basal texture). Their basal orientations were confirmed by the corresponding (0002) pole figure in Fig. 5(b). This indicated

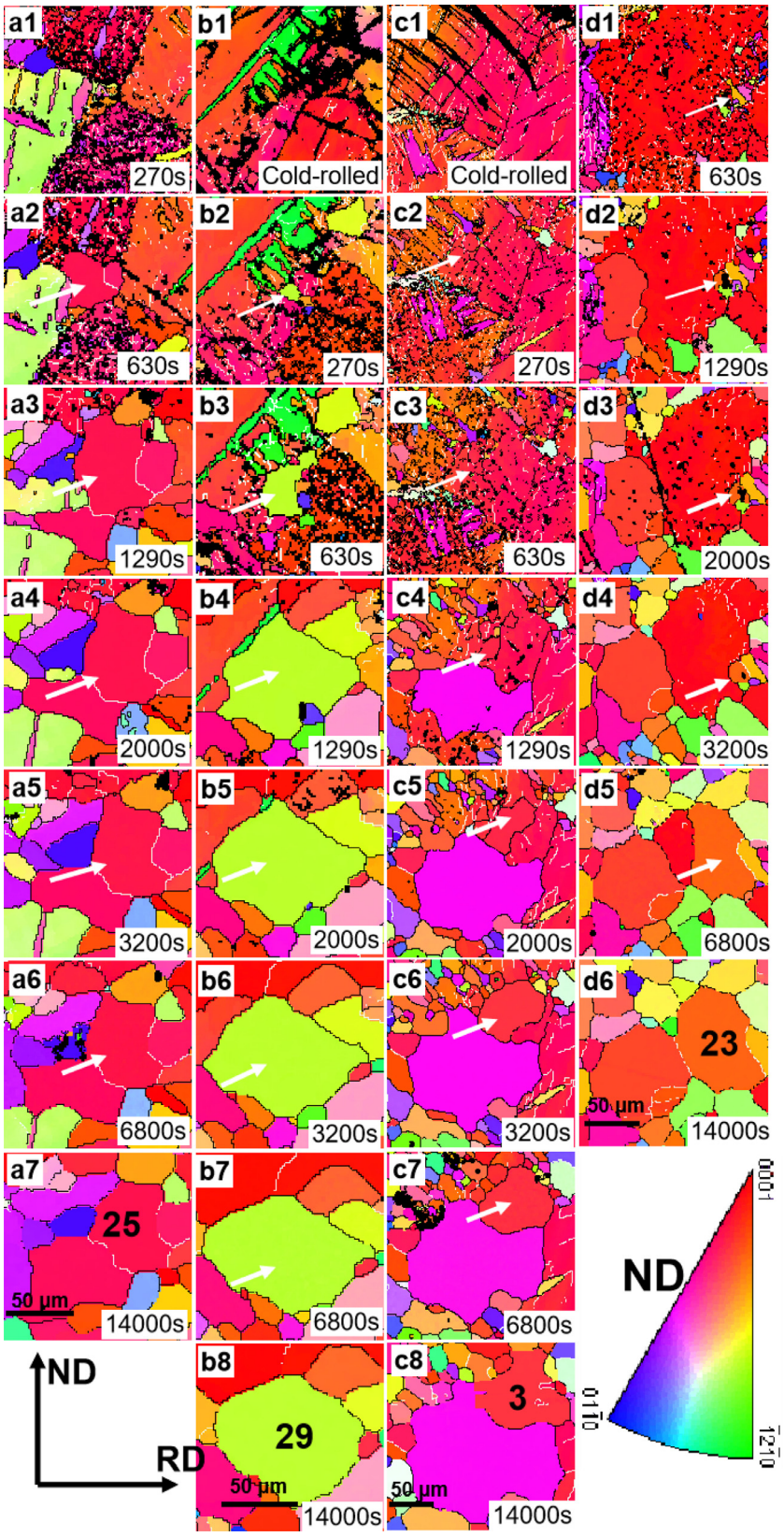

Fig. 3. Nucleation and growth behaviour of 4 typical recrystallised grains originated from (a1–a7) deformed grain boundaries, (b1–b8) shear bands, (c1–c8) double twin networks, and (d1–d6) a second phase particle.

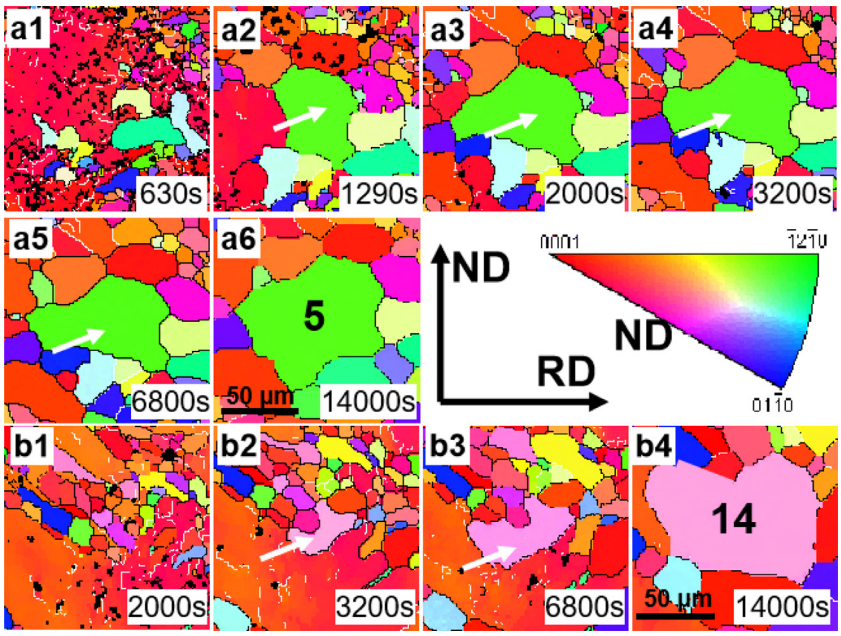

Fig. 4. Nucleation and growth behaviour of 2 typical recrystallised grains originated from deformed grain interiors: (a1–a6) grain 5 emerged at an early stage and (b1–b4) grain 14 at the late stage of the recrystallisation process.

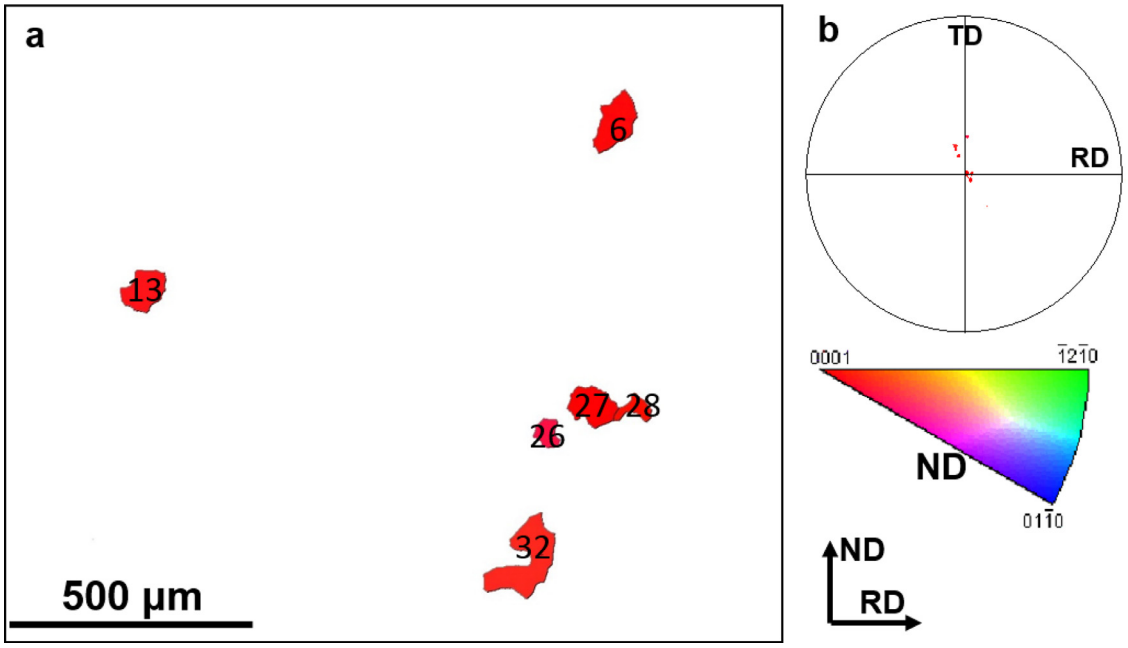

Fig. 5. (a) EBSD IPF subset map only showing the basal grains in sample SCA350 after 14,000 s annealing and (b) its corresponding scattered (0002) pole figure.

the nucleation and growth of basal orientated coarse grains did not dominate the whole recrystallisation process.

4. Conclusions

In summary, this work fully disclosed the nucleation and grain growth mechanism of coarse grains observed in a Mg AZ31B alloy during the whole recrystallisation process at the annealing temperature of 350 °C by using the quasi-*in-situ* EBSD method. The main conclusions were drawn:

(1) The basal texture intensity of SCA350 sample was significantly weakened compared to as-received AZ31B sample. The coarse grains of SCA350 only slightly enhanced its basal texture intensity after annealing 14,000 s. Thus, further annealing this sample might result in the formation of basal texture components due

to further grain growth of coarse grains with basal orientations.

(2) The orientations of all the 34 coarse grains were quite different. Their first appearance during recrystallisation ranged from 270 s to 6800 s. No orientated grain growth or special type of grain boundaries were observed amongst these 34 coarse grains.

(3) 20 of 34 coarse grains were originated from subgrains nucleated by AsGG. Their rapid grain growth could be attributed to the large adjacent deformed parent grain around the nucleated grains. The growth rate was significantly decreased when the recrystallised grains meet other recrystallised grains

(4) 28 of 34 coarse grains had non-basal orientations, especially coarse grains nucleated by AsGG. Thus, activating AsGG recrystallisation could be an effective route to largely weaken the basal texture intensity and improve formability of conventional Mg alloys (e.g., AZ series alloys), which will expand their applications in several industrial sectors.

Declaration of Competing Interest

The authors declare that they have no known competing financial interests or personal relationships that could have appeared to influence the work reported in this paper.

Acknowledgments

This work was supported by the UKRI MRC Future Leaders Fellowship, MR/T019123/1. We wish to acknowledge the Henry Royce Institute for Advanced Materials, funded through EPSRC grants EP/R00661X/1, EP/S019367/1, EP/P02470X/1 and EP/P025285/1, for JSM-7900F FE-SEM/EBSD kit access at The University of Sheffield.

Supplementary materials

Supplementary material associated with this article can be found, in the online version, at doi:10.1016/j.jma.2021.08.026.

References

[1] B. Srinivasarao, N.V. Dudamell, M.T. Pérez-Prado, Mater. Charact. 75 (2013) 101–107.
[2] D. Griffiths, Mater. Sci. Technol. 31 (2015) 10–24.
[3] A. Imandoust, C.D. Barrett, T. Al-Samman, K.A. Inal, H. El Kadiri, J. Mater. Sci. (2016) 1–29.
[4] J. Kuang, X. Du, T. Al-Samman, X. Li, G. Liu, J. Sun, Metall. Mater. Trans. A 51 (2020) 6640–6657.
[5] D. Guan, X. Liu, J. Gao, L. Ma, B. Wynne, W.M. Rainforth, J. Alloy. Compd. 774 (2019) 556–564.
[6] D. Guan, X. Liu, J. Gao, L. Ma, B.P. Wynne, W.M. Rainforth, Sci. Rep. 9 (2019) 7152.
[7] D. Guan, W.M. Rainforth, J. Gao, J. Sharp, B. Wynne, L. Ma, Acta Mater. 135 (2017) 14–24.
[8] Z.R. Zeng, Y.M. Zhu, S.W. Xu, M.Z. Bian, C.H.J. Davies, N. Birbilis, J.F. Nie, Acta Mater. 105 (2016) 479–494.
[9] K. Hantzsche, J. Bohlen, J. Wendt, K.U. Kainer, S.B. Yi, D. Letzig, Scr. Mater. 63 (2010) 725–730.
[10] J.F. Nie, K.S. Shin, Z.R. Zeng, Metall. Mater. Trans. A 51 (2020) 6045–6109.
[11] N. Stanford, Mater. Sci. Eng. A 565 (2013) 469–475.
[12] J.J. Bhattacharyya, S.R. Agnew, G. Muralidharan, Acta Mater. 86 (2015) 80–94.
[13] M.A. Steiner, J.J. Bhattacharyya, S.R. Agnew, Acta Mater. 95 (2015) 443–455.
[14] S.A. Farzadfar, É. Martin, M. Sanjari, E. Essadiqi, S. Yue, J. Mater. Sci. 47 (2012) 5488–5500.
[15] S.A. Farzadfar, É. Martin, M. Sanjari, E. Essadiqi, M.A. Wells, S. Yue, Mater. Sci. Eng. A 534 (2012) 209–219.
[16] X. Huang, K. Suzuki, Y. Chino, M. Mabuchi, J. Alloy. Compd. 509 (2011) 7579–7584.
[17] X. Huang, K. Suzuki, Y. Chino, M. Mabuchi, J. Mater. Sci. 47 (2012) 4561–4567.
[18] R. Pei, S. Korte-Kerzel, T. Al-Samman, J. Mater. Sci. Technol. 50 (2020) 257–270.
[19] J. Humphreys, G.S. Rohrer, A. Rollett, Chapter 7 - recrystallization of single-phase alloys, in: J. Humphreys, G.S. Rohrer, A. Rollett (Eds.), Recrystallization and Related Annealing Phenomena, (3rd ed.), Elsevier, Oxford, 2017, pp. 245–304.
[20] D. Guan, W.M. Rainforth, L. Ma, B. Wynne, J. Gao, Acta Mater. 126 (2017) 132–144.
[21] D. Guan, W.M. Rainforth, J. Gao, L. Ma, B. Wynne, Acta Mater. 145 (2018) 399–412.
[22] M.R. Barnett, M.D. Nave, C.J. Bettles, Mater. Sci. Eng. A 386 (2004) 205–211.
[23] E.A. Holm, M.A. Miodownik, A.D. Rollett, Acta Mater. 51 (2003) 2701–2716.
[24] M. Ferry, F.J. Humphreys, Acta Mater. 44 (1996) 1293–1308.
[25] F.J. Humphreys, Acta Mater. 45 (1997) 4231–4240.
[26] Y. Huang, F.J. Humphreys, M. Ferry, Acta Mater. 48 (2000) 2543–2556.
[27] S.R. Ahl, H. Simons, C. Detlefs, D.J. Jensen, H.F. Poulsen, Acta Mater. 185 (2020) 142–148.
[28] J. Tang, L. Chen, Z. Li, G. Zhao, C. Zhang, Corros. Sci. 180 (2021) 109201.